Fully resolved simulation of dense suspensions of freely evolving buoyant particles using an improved immersed boundary method

Vahid Tavanashad[a,b], Shankar Subramaniam[a,b,*]

[a]*Department of Mechanical Engineering, Iowa State University, Ames, IA 50011, USA*
[b]*Center for Multiphase Flow Research & Education (CoMFRE), Iowa State University, Ames, IA 50011, USA*

Abstract

Fully resolved simulation of flows with buoyant particles is a challenging problem since buoyant particles are lighter than the surrounding fluid, and as a result, the two phases are strongly coupled together. In this work, the virtual force stabilization technique introduced by Schwarz et al. [Schwarz, S., Kempe, T., & Fröhlich, J. (2015). A temporal discretization scheme to compute the motion of light particles in viscous flows by an immersed boundary method. J. Comput. Phys., 281, 591–613] is extended to simulate buoyant particle suspensions with high volume fractions (up to 40%). It is concluded that the dimensionless numerical model constant C_v in the virtual force technique should increase with volume fraction. The behavior of a single rising particle, two in-line rising particles, and buoyant particle suspensions are studied. In each case, results are compared with experimental works on bubbly flows to highlight the differences and similarities between buoyant particles and bubbles. Finally, the drag coefficient is extracted from simulations of buoyant particle suspensions at different volume fractions, and based on that a drag correlation is presented.

*Corresponding author
Email address: shankar@iastate.edu (Shankar Subramaniam)

1. Introduction

Free fall and rise of solid particles in a fluid is a type of dispersed multiphase flow. This type of flow is of interest in numerous fields, including chemical, mechanical, and environmental engineering. In particular, many types of microplastics, such as polyethylene and polypropylene, are considered buoyant in the oceans unless they are altered by biofilm growth [1, 2]. Besides, the simulation of buoyant particles can be used as an approximation for bubbles under certain conditions. An important factor that affects the flow physics in bubbly flows is the purity of the surrounding liquid [3–5]. It is shown in many experimental studies [6–10] that the rise velocity of a single bubble is significantly higher in clean systems, such as pure water, when compared to contaminated systems, such as tap water, especially in parameter ranges where the shape of the bubble is spherical or ellipsoidal. Moreover, these studies show that small spherical bubbles in contaminated systems behave like solid spheres. This means that the simulation of bubbles with the no-slip velocity boundary condition at the interface of two phases, instead of free-slip, is a good approximation of contaminated bubbly flows.

Fully-resolved direct numerical simulations (FR-DNS) of particle-laden flows are used as a tool for discovering flow physics as well as model development for macro-scale simulations such as Eulerian–Eulerian or Eulerian–Lagrangian approaches [11]. Therefore, it is necessary to develop numerical methods capable of simulating systems that span a wide range of particle-to-fluid density ratios from heavy to light particles. Over time, different numerical methods have been developed and improved for FR-DNS of particle-laden flows such as immersed boundary [12–15], lattice Boltzmann [16–20], fictitious domain with Lagrange multipliers [21–25], PHYSALIS [26, 27], and body-fitted [28–31] methods. In these methods, the motion of particles is determined by Newton's equations of

motion.

When loose coupling schemes are used in these methods, the interface boundary conditions may not be satisfied accurately since these schemes only involve the solution of the fluid and the particle, once per time step. This incompatibility of the kinematic and dynamic quantities at the interface may cause severe stability issues when the particle density ρ_p is close to, or smaller than, the fluid density ρ_f [12, 14, 15, 20, 25, 32–34]. This numerical instability is known as artificial added-mass effects of the fluid on the particle, and is common in fluid–structure interaction problems [35–38]. Although the use of strong coupling methods (implicit coupling schemes) solves the instability problem at the expense of computational time [28, 39, 40], numerous studies have attempted to stabilize explicit coupling schemes to overcome the problem and benefit from the simplicity of explicit methods [25, 41–43].

In the present study, we develop a stabilized explicit coupling scheme for FR-DNS using the immersed boundary method (IBM) that is capable of simulating buoyant rigid particles. Several studies have shown that the IBM becomes unstable for low particle-to-fluid density ratios when explicit methods are used. [12, 14, 15, 33, 34]. For instance, the IBM developed by Uhlmann [12] becomes unstable when the density ratio ρ_p/ρ_f is smaller than 1.2. To extend the stability range, Kempe and Fröhlich [14] succeeded in performing simulations with density ratio as low as 0.3 by numerical evaluation of volume integrals in the equation of particle motion, instead of using the rigid-body motion assumption (assuming that the fictitious fluid motion inside the particle is equal to rigid-body motion irrespective of the actual type of motion inside the volume) made by Uhlmann. Yang and Stern [33] utilized the rigid-body assumption but used a 4th-order predictor-corrector scheme to solve the equation of motion for particles and achieved stable solution for $\rho_p/\rho_f > 0.29$. Our implementation of IBM [13, 44] which is called the particle-resolved uncontaminated-fluid reconcilable immersed boundary method (PUReIBM) directly calculates the hydrodynamic force on particle surface from the stress field, and it is stable for $\rho_p/\rho_f > 0.07$ (see section 4.1.1).

3

While the works of Kempe and Fröhlich [14] and Yang and Stern [33] "improve" the stability limit, Tschisgale et al. [45] have developed a non-iterative implicit IBM to "remove" the low-density ratio restriction and they successfully simulated a single rising particle with density ratio 0.001. Another promising work for removing the low-density ratio restriction is done by Schwarz et al. [46]. In their work, a virtual force stabilization technique is introduced, which allows simulation of a single rising particle with density ratio as low as 0.001. In this technique, the governing equations are solved using an explicit method, and a virtual force is added to the equation of particle motion to stabilize the method. This idea was originally used for a single rising particle and later was used for very dilute systems of contaminated bubble swarms with volume fraction up to 2.14% [47]. The focus of the work by Schwarz et al. [46] is on numerical accuracy. They tried to design a numerical scheme with the same accuracy as their original method without the virtual force. The virtual force method has a dimensionless numerical model constant C_v, which represents the magnitude of the dimensionless virtual force in the particle equation of motion, and Schwarz et al. [46] claimed that this method works for any C_v greater than zero.

In this paper, we show that there is a lower positive limit for C_v, which depends on the density ratio and the added mass coefficient. This condition is essential in the case of buoyant particle suspensions compared to a single particle because the added mass coefficient is affected by the volume fraction. Therefore, it is important to choose a C_v that results in stable solutions for buoyant particle suspensions. The ultimate goal of this work is to develop an explicit time-stepping method that simulates buoyant particles for arbitrary density ratio and a range of volume fractions. In this regard, the results of a single rising particle are presented for validation. Then, the behavior of two in-line rising particles is studied. Finally, the drag coefficient is extracted from simulations of buoyant particle suspensions at different volume fractions, as an illustrative example to show the applicability of this method in practice. In each part, results are compared with experimental works on bubbly flows to highlight the differences and similarities between buoyant particles and bubbles. Based

4

on the data obtained from simulations of buoyant particle suspensions, we have also proposed a correlation for the drag coefficient of particle suspension to show the application of our modified FR-DNS solver for model development.

Although in this study we use IBM to solve the governing equations, the virtual force stabilization technique is not restricted to IBM and could be used in any flow solver in which the motion of bubbles or buoyant particles is determined by Newton's equations of motion. For instance, Xia et al. [48] used this technique to modify the direct-forcing fictitious domain method for particle-laden flows of arbitrary density ratio and dilute systems with volume fraction up to 0.84%.

The rest of the paper is organized as follows: In section 2, the underlying reason for instability in the simulations of buoyant particles is explained. Then the virtual force stabilization technique is introduced, and a detailed explanation is provided as to why and how it works. In section 3, the IBM used in this work is introduced, and modifications required of the original method to incorporate the virtual force are explained. In section 4, the new method is validated, and simulation results for dense buoyant particle suspensions are presented. Finally, conclusions are drawn in section 5.

2. Numerical instability in simulations of strongly coupled particle-fluid flows

Although the final goal of this study is to perform FR-DNS, for simplicity, the instability problem that occurs in low-density-ratio simulations is first explained through point particle equations in sections 2.1 and 2.2. The virtual force stabilization approach is easier to explain in the point-particle context because the added mass force appears explicitly, whereas in FR-DNS it is a part of the integral of fluid stress at the particle surface. The extension to FR-DNS is discussed in section 2.3.

2.1. Explanation of the stability problem in point-particle simulations

In the point-particle approach, the interaction between particles and the surrounding flow is modeled. In this case, the equation of motion for particles

5

is described using the Basset-Boussinesq-Oseen (BBO) equation,

$$m_p \frac{d\mathbf{V}}{dt} = \mathbf{F}_D + \mathbf{F}_L + \mathbf{F}_{AM} + \mathbf{F}_{BH} + \mathbf{F}_B, \tag{1}$$

where $\mathbf{V}$ is the particle velocity, m_p is the particle mass, $\mathbf{F}_D$ denotes the drag force, $\mathbf{F}_L$ the lift force, $\mathbf{F}_B$ the body forces, $\mathbf{F}_{AM}$ the added mass force and $\mathbf{F}_{BH}$ the Basset history force.

In this equation, the added mass force is defined as:

$$\mathbf{F}_{AM} = m_{am} \left(\frac{D\mathbf{u}}{Dt} - \frac{d\mathbf{V}}{dt} \right), \tag{2}$$

where $\mathbf{u}$ is the fluid velocity at the particle location and m_{am} is the added mass which is usually defined by a dimensionless coefficient C_{am} as $m_{am} = C_{am}\rho_f V_p$, where ρ_f is density of fluid and V_p is volume of particle. Added mass represents the inertia added to a particle as it accelerates (or decelerates) and moves (or deflects) a portion of its surrounding fluid.

Hu et al. [28] have shown that Eq. (1) is unstable when it is solved with an explicit time integration method, and the added mass exceeds the particle mass. They assume that at the early stages of motion, only body forces and added mass force are important. Furthermore, they assume that at the early stages, the fluid acceleration is much smaller than the particle acceleration. Under these assumptions, Eq. (1) simplifies to:

$$m_p \frac{d\mathbf{V}}{dt} = \mathbf{F}_B - m_{am} \frac{d\mathbf{V}}{dt}. \tag{3}$$

Note that $\mathbf{F}_B = (\rho_p - \rho_f) V_p \mathbf{g}$ is a constant driving force (ρ_p is particle density and $\mathbf{g}$ is the acceleration due to the gravity). Starting from an initial condition and solving this equation explicitly for the next time step, it can be shown that acceleration at time step n is related to the initial acceleration through the following equation [28],

$$\frac{d\mathbf{V}}{dt}(t_n) = \frac{1 - \left(-\frac{m_{am}}{m_p}\right)^n}{m_p + m_{am}} \mathbf{F}_B - \left(-\frac{m_{am}}{m_p}\right)^n \frac{d\mathbf{V}}{dt}(t_0). \tag{4}$$

Equation (4) shows that the particle velocity oscillates with increasingly large amplitude when the added mass is larger than the mass of particle. Therefore,

6

the stability condition for Eq. (4) is:

$$m_p > m_{am} \Rightarrow \rho_p/\rho_f > C_{am}, \tag{5}$$

which means density ratio should be greater than the added mass coefficient to have stable solution. In the next subsection, we describe how to remove this instability condition.

2.2. Solving the instability problem using the virtual force technique

Schwarz et al. [46] introduced the virtual force technique to stabilize the equation of motion for particles in the case of low-density ratio. They defined the virtual force as:

$$\mathbf{F}_v = C_v \rho_f V_p \frac{d\mathbf{V}}{dt}, \tag{6}$$

with C_v an appropriately chosen coefficient. Although the virtual force is defined similar to the added mass force, it is a purely mathematical term designed to stabilize the temporal integration and does not have any physical meaning.

Schwarz et al. [46] added the virtual force to a "generic" test case which excluded the added mass force and concluded that $C_v > 0$. Here, we add the virtual force to Eq. (3) which includes the added mass force and show that there is a lower positive limit for C_v. Starting with Eq. (3) and adding the virtual force to this equation results in:

$$m_p \frac{d\mathbf{V}}{dt} + \mathbf{F}_v = \mathbf{F}_B - m_{am} \frac{d\mathbf{V}}{dt} + \mathbf{F}_v. \tag{7}$$

By defining $m_p^{eq} = m_p + C_v \rho_f V_p$ and $m_{am}^{eq} = m_{am} - C_v \rho_f V_p$, this equation is re-written as:

$$m_p^{eq} \frac{d\mathbf{V}}{dt} = \mathbf{F}_B - m_{am}^{eq} \frac{d\mathbf{V}}{dt}. \tag{8}$$

It is clear that Eqs. (3) and (8) are similar and we conclude that the latter equation is only stable if $m_p^{eq} > m_{am}^{eq}$ which simplifies to:

$$\frac{m_p^{eq}}{m_{am}^{eq}} > 1 \Rightarrow \frac{\rho_p + C_v \rho_f}{(C_{am} - C_v)\rho_f} > 1 \Rightarrow C_v > \frac{C_{am}}{2} - \frac{\rho_p}{2\rho_f}. \tag{9}$$

This result shows that there is a lower limit for C_v which we call C_v^{min}, and it depends on the added mass coefficient and the density ratio.

7

It is known that the geometry of a particle and the presence of other particles or bounding walls can affect the added mass coefficient [49], so it is expected that the physics of the problem affects the stability condition on C_v through the added mass coefficient, which is confirmed in section 4.3 where we simulate buoyant particle suspensions.

2.3. Using the virtual force technique in fully resolved simulations

In FR-DNS, particles are fully resolved by the grid, and the flow field on the surface of each particle is captured by solving the Navier-Stokes equations. The hydrodynamic force on each particle is calculated by integrating the pressure and viscous stress fields over the particle surface, and the resulting equation of motion for each particle is,

$$m_p \frac{d\mathbf{V}}{dt} = \mathbf{F}_h + \mathbf{F}_B, \tag{10}$$

where $\mathbf{F}_h = \oint_{\Gamma_p} \boldsymbol{\tau} \cdot \mathbf{n} ds$ is the hydrodynamic force, $\boldsymbol{\tau} = -\mathbf{I}p + \mu_f \left(\nabla \mathbf{u} + \nabla \mathbf{u}^T\right)$ is the hydrodynamic stress tensor, $\mathbf{I}$ the identity matrix, μ_f the fluid dynamic viscosity, p is the pressure with the hydrostatic part being subtracted, and $\mathbf{n}$ is the normal vector at the surface of particle.

As mentioned in the Introduction, the solution of this equation also becomes problematic for low-density ratios as reported in the literature [12, 14, 15, 33, 34]. Similarly, our code, PUReIBM, also becomes unstable for low-density ratios, but only for $\rho_p/\rho_f < 0.07$. Therefore, it is proposed to apply the virtual force technique in PUReIBM to stabilize the fully resolved simulations for low-density ratios, which is the topic of section 3. Before explaining the detail of PUReIBM, we emphasize a few points about the virtual force technique:

1. In FR-DNS, the surface integral in Eq. (10) is evaluated directly from the flow field yielding all forces introduced in Eq. (1) acting on the particle.

2. Since Eq. (10) inherently includes the added mass force, the virtual force technique can be used to stabilize this equation with a $C_v > C_v^{min}$.

3. The value of C_v^{min} is not necessarily exactly the same as found in Eq. (9) since Eqs. (7) and (10) are different. However, C_v^{min} still depends on the

added mass coefficient and density ratio (more detail about this point is presented in section 4).

4. The virtual force technique can be used to stabilize any explicit numerical method that solves Eq. (10) coupled with fluid equations for low-density ratios and is not limited to IBM.

3. Numerical method for FR-DNS

The fully resolved simulation approach used in this work is based on the direct forcing immersed boundary method of Mohd-Yusof [50] which is further developed in [13, 44], and is called the particle-resolved uncontaminated-fluid reconcilable immersed boundary method (PUReIBM). The PUReIBM methodology is explained in detail in other works [13, 51, 52] and has been extensively validated in different cases [44, 52, 53]. Here, the main features of this method are presented.

The governing equations of the fluid phase that are solved in PUReIBM are the continuity equation:

$$\boldsymbol{\nabla} \cdot \mathbf{u} = 0, \tag{11}$$

and the Navier-Stokes equations:

$$\rho_f \frac{\partial \mathbf{u}}{\partial t} + \rho_f \boldsymbol{\nabla} \cdot (\mathbf{uu}) = -\nabla p + \mu_f \nabla^2 \mathbf{u} + \mathbf{f}_{\text{IBM}}, \tag{12}$$

which are solved on a uniform Cartesian grid points with the Crank-Nicolson scheme for the viscous terms and an Adams-Bashforth scheme for the convective terms. The boundary conditions on the fluid velocity at the particle interface (no-slip and no-penetration) are imposed via the immersed boundary force term, $\mathbf{f}_{\text{IBM}}$.

The motion of each particle in PUReIBM is evolved by updating its position $\mathbf{X}$, translational velocity $\mathbf{V}$, and rotational velocity $\boldsymbol{\Omega}$ according to Newton's

second law as:

$$\frac{d\mathbf{X}}{dt} = \mathbf{V}, \tag{13}$$

$$m_p \frac{d\mathbf{V}}{dt} = \mathbf{F}_B + \mathbf{F}_h + \sum_{\substack{j=1 \\ j \neq i}}^{N_p} \mathbf{F}_c^{(ij)}, \tag{14}$$

$$I_p \frac{d\mathbf{\Omega}}{dt} = \mathbf{T}_h + \sum_{\substack{j=1 \\ j \neq i}}^{N_p} \mathbf{T}_c^{(ij)}, \tag{15}$$

where N_p is the number of particles, $\mathbf{F}_c^{(ij)}$ is the collisional force between the ith particle and j^{th} particle, $I_p = 1/10\rho_p V_p d_p^2$ is the moment of inertia of particles, d_p is the particle diameter, $\mathbf{T}_h$ is the hydrodynamic torque, and $\mathbf{T}_c$ is the collisional torque.

A soft-sphere collision [54] is used to model the particle-particle interactions. Particles are allowed to overlap during a collision, and the contact mechanics between the overlapping particles are modeled by a spring in the normal direction (elastic collisions). The spring causes the colliding particles to rebound. The particles considered in this study are assumed to be frictionless. This implies that the tangential component of the contact force and $\mathbf{T}_c$ are zero.

In the next sections 3.1 and 3.2, the modifications to the original PUReIBM to extend its capability to simulate buoyant particles are explained.

3.1. Addition of virtual force and torque to PUReIBM

Since Eq. (14) is solved explicitly for the particle acceleration in PUReIBM, some numerical instabilities arise in the code when the density ratio is small. As discussed in the previous section, the virtual force (Eq. (6)) should be added to both sides of Eq. (14) to stabilize the PUReIBM for low-density ratio simulations,

$$(m_p + C_v \rho_f V_p) \frac{d\mathbf{V}}{dt} = \mathbf{F}_B + \mathbf{F}_h + \sum_{\substack{j=1 \\ j \neq i}}^{N_p} \mathbf{F}_c^{(ij)} + \mathbf{F}_v. \tag{16}$$

Similar to the concept of virtual force, we can define a virtual torque $\mathbf{T}_v = 1/10\, C_v^T \rho_f V_p d_p^2 \dfrac{d\mathbf{\Omega}}{dt}$ and add it to both sides of Eq. (15) to stabilize this equation,

$$\left(I_p + \frac{1}{10}\, C_v^T\, \rho_f V_p d_p^2\right) \frac{d\mathbf{\Omega}}{dt} = \mathbf{T}_h + \sum_{\substack{j=1 \\ j\neq i}}^{N_p} \mathbf{T}_c^{(ij)} + \mathbf{T}_v. \tag{17}$$

In the definition of virtual torque, C_v^T is the virtual torque coefficient and it is considered to be equal to C_v in this paper.

A combination of the Adams-Bashforth predictor-corrector scheme and the trapezoidal rule (see Appendix A) is used to calculate $\mathbf{F}_v$ and $\mathbf{T}_v$ on the right-hand side of Eqs. (16) and (17), which is necessary for having the same order of convergence as the original method without virtual force as discussed in [46]. Also, we follow the same initialization approach used in [46]. The overall order of accuracy and convergence properties of the modified method and the temporal and spatial discretization errors are not changed by adding the virtual force, as mentioned in [46], so a discussion on these topics is not repeated here.

3.2. Lubrication force

In numerical methods based on structured grids such as IBM, the flow field is not accurately resolved when the distance between the surface of particles becomes less than the grid spacing. Therefore, the lubrication force is not completely resolved, which is important, especially in buoyant particles. To resolve the lubrication force, it is necessary to use a fine grid, which results in very small time steps for the explicit scheme used here. However, it has been argued in the literature that the details of the lubrication and collision model are only important when the trajectory of an individual particle is investigated, while the average statistics of large systems are not affected by these details [55, 56].

In this work, the lubrication force is modeled as [27, 57]:

$$\mathbf{F}_{lub}^{ij} = \begin{cases} 0 & h < \epsilon_{col} \\ -6\pi\mu_f \dfrac{d_p^2}{16}\left(\dfrac{1}{h} - \dfrac{1}{\epsilon_{lub}}\right)\mathbf{U}_{ij}\cdot\mathbf{n}_{ij} & \epsilon_{col} < h < \epsilon_{lub} \\ 0 & h > \epsilon_{lub} \end{cases} , \qquad (18)$$

where $\mathbf{F}_{lub}^{ij}$ is the lubrication force, $\mathbf{U}_{ij}$ is relative velocity between particle i and j, $\mathbf{n}_{ij}$ is unit vector pointing out from the center of particle i to the center of particle j, $h = |\mathbf{x}_i - \mathbf{x}_j| - d_p$ is the surface-to-surface distance between particles i and j, ϵ_{lub} is the cutoff distance beyond which the lubrication force is negligible and ϵ_{col} has a nonzero positive value to prevent the singularity in the lubrication force as $h \to 0$. Even with the inclusion of the lubrication force, some particles may collide with each other. In this case, we use the same collision model already introduced, but with a small change that the collision starts when $h < \epsilon_{col}$, which prevents the lubrication force from becoming singular. The parameters of lubrication force used in this study are $\epsilon_{lub}/d_p = 0.5$ and $\epsilon_{col}/d_p = 0.0003$, as suggested in the literature [27, 55, 57].

4. Results and discussion

In this section, the simulation of a single buoyant particle is presented first, with the goal of the validation. Then, the rise of two in-line buoyant particles is presented and compared with experimental results. Finally, simulations of buoyant particle suspensions at different volume fractions are presented, and a drag law for buoyant particle suspensions is proposed based on the results of this part.

4.1. Rise of a single buoyant particle

The goal of this subsection is to show that the implementation of the virtual force in PUReIBM is done correctly and to validate the numerical simulation. Two different comparisons are made with other numerical and experimental works in the literature. In the first case, the temporal evolution of particle

12

velocity is studied, and results are compared with other numerical works. Then, the drag force on a single buoyant particle is compared with the drag on a spherical bubble in contaminated liquid from an experiment.

4.1.1. Temporal evolution

In this subsection, the motion of a single sphere ascending in a quiescent, viscous fluid under the action of gravity is simulated. The input dimensionless parameters are Archimedes number Ar and density ratio ρ_p/ρ_f. The Archimedes number is defined as:

$$Ar = \frac{\rho_f|\rho_p - \rho_f|gd_p^3}{\mu_f^2}. \tag{19}$$

The simulation is performed in a cuboidal domain with periodic boundary conditions in all directions. The length of the domain in the direction of gravity is $L_x = 12.8d_p$, which is twice the length of the domain in other directions. The particle and fluid are initially at rest and evolve under the action of gravity. A mean pressure gradient is imposed on the system to oppose gravity and keep the mean fluid velocity zero, and then the particle starts to move due to the buoyant force. Although a condition for C_v^{min} was derived in Eq. (9) for the case of point particle simulations, other parameters affect C_v^{min} in fully resolved simulations such as the grid resolution. For example, the lowest density ratio that can be simulated in PUReIBM (without using virtual force stabilization) is $\rho_p/\rho_f = 0.09$ with grid resolution per particle diameter $D_m = 20$ and $\rho_p/\rho_f = 0.07$ with $D_m = 30$. The C_v^{min} for these two cases are 0.15 and 0.11, respectively. In our simulations, $C_v = 0.15$ is used for the case of a single particle.

Figure 1 shows the region of stability for the simulation of a single rising particle with $Ar = 1000$ and $D_m = 20$. Simulations are unconditionally unstable for C_v less than C_v^{min} independent of the grid resolution and time step. This figure also shows that the simulations are stable for $C_v > C_v^{min}$, however, to get accurate results, it is necessary to limit the time step. In the single rising particle simulation under gravity, the velocity at the beginning is very small, and using a constant $CFL = u_{max}\Delta t/\Delta x$ will result in a large time step. Therefore a constant time step is used in PUReIBM with a condition on the maximum CFL

13

number. If the CFL number becomes larger than the maximum CFL number, then the time step is decreased. For the case shown in Fig. 1, the CFL number does not become larger than the maximum CFL number, and hence the time step remains constant during the simulation.
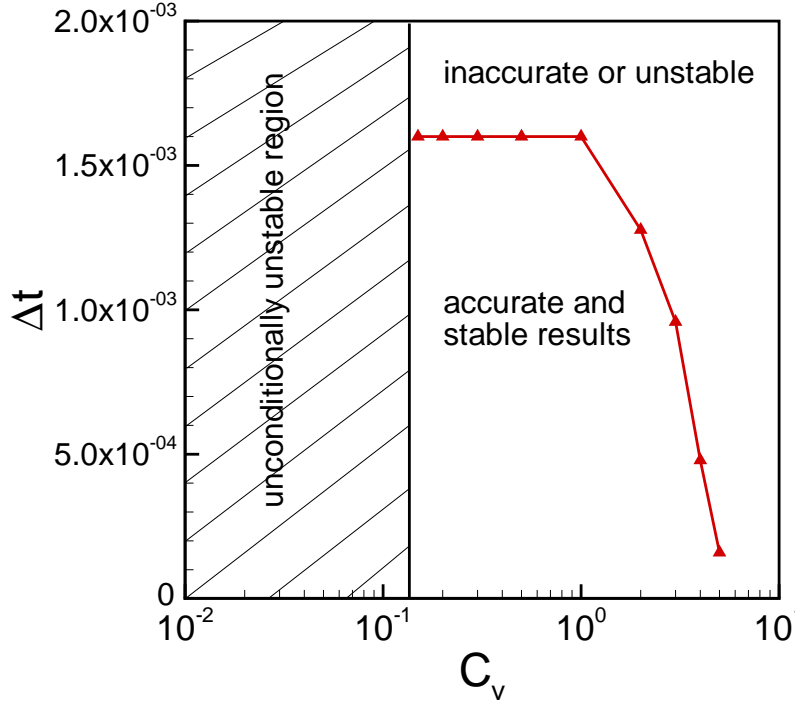

Figure 1: Stability region for the simulation of a single rising particle for $D_m = 20$. Simulations are unconditionally unstable for C_v less than $C_v^{min} = 0.15$ independent of the grid resolution and time step. The simulations are stable for $C_v > C_v^{min}$, however, to get accurate results it is necessary to limit the time step.

To validate the result for the rise velocity of a single particle, it is compared with the numerical simulation using IBM developed by Schwarz et al. [46] and an implicit, highly-resolved spectral body-fitted method developed in Dušek's group [58, 59]. The results from Dušek's group were received by Schwarz et al. [46] in private communication and are published in their work.
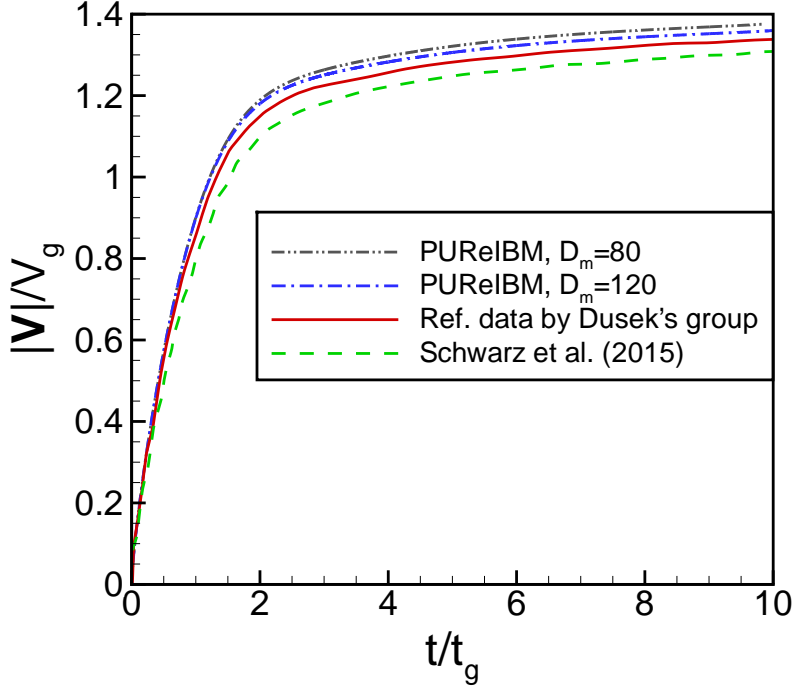
Figure 2: Temporal evolution of a single rising particle for $Ar = 28900$ and $\rho_p/\rho_f = 0.001$. Results of PUReIBM with two grid resolutions are compared to the reference body-fitted simulation of Dušek's group [58, 59] and the IBM simulation of Schwarz et al. [46].

This comparison is shown in Fig. 2 for $\rho_p/\rho_f = 0.001$ and $Ar = 28900$. For the comparison, the gravitational velocity and time scale are utilized as reference values:

$$V_g = \sqrt{|\rho_p/\rho_f - 1|gd_p}, \qquad t_g = \sqrt{\frac{d_p}{|\rho_p/\rho_f - 1|g}}.$$

The results of PUReIBM are shown for two different grid resolutions in this figure. At the early time, the PUReIBM results match very well with the reference result of Dušek's group. However, the terminal velocity is slightly different. The difference decreases with increasing grid resolution, but convergence to the reference result is slow. Similarly, the IBM results of Schwarz et al. [46] deviates from the reference terminal velocity. In IBM, the no-slip and no-penetration velocity boundary conditions on the particle surface are imposed on Lagrangian

marker points through the immersed boundary force and then spread to the Cartesian grid using a regularized delta function. In the implementation of IBM that is used by Schwarz et al. [46], the Lagrangian marker points are on the surface of the particle, and the immersed boundary force is spread into the fluid domain, while in PUReIBM the Lagrangian marker points are inside the particle and the immersed boundary force is restricted to Eulerian grid points lying inside the sphere, while the fluid domain is uncontaminated by the immersed boundary force. This could explain why the terminal velocity results of Schwarz et al. [46] are smaller than the reference data, and the results of PUReIBM are larger.

Note that only the beginning of the acceleration phase is considered for comparison in Fig. 2, which is before the particle path shows instability [59]. When the Reynolds number is higher than a critical value, and the particle density is much smaller than that of the surrounding fluid, the particle motion is spiral, and the drag coefficient is almost constant. At Reynolds number below the critical value, the drag coefficient follows the standard drag curve and the trajectory is linear[58–63]. This behavior is explained as the mechanical inertia of the particle becomes small enough for the wake to induce rotation of the particle, thus creating a spiral trajectory [60]. In addition, for light particles, the dominant inertial force is the added mass from the attached fluid, which accelerates with the particle. This effect is shown recently to play an important role in the dynamics of buoyant particles suspensions [56].

Another interesting test case for buoyant particles is the rise of a buoyant particle in an inclined channel. In this problem, the particle rises in an inclined channel due to buoyancy and travels alongside the right wall of the domain. Lomholt et al. [64] have performed an experiment for this case for a particle with $\rho_p/\rho_f = 0.97$. However, PUReIBM works properly, even without the virtual force stabilization technique for this density ratio. In other words, the results with and without virtual force stabilization would be the same for $\rho_p/\rho_f = 0.97$. Therefore we have presented this test case in Appendix B.

4.1.2. Drag coefficient of a single buoyant particle

As another validation, the results of PUReIBM for the drag coefficient of a single rising particle are compared with the experimental results of [9]. The experimental work reports the drag of nearly spherical gaseous bubbles (aspect ratio $E > 0.95$) in tap (contaminated) water. As explained already, buoyant particles are a good approximation for bubbles in contaminated liquid, so this comparison is valid.

Additionally, the results are compared with the drag correlation for a single bubble in an unbounded medium of contaminated liquid proposed by Tomiyama et al. [65]. This correlation is expressed as:

$$C_{d,0} = \max\left[\frac{24}{Re}\left(1 + 0.15Re^{0.687}\right), \frac{8}{3}\frac{Eo}{Eo+4}\right], \tag{20}$$

where Eo is Eötvös number which represents the ratio between buoyancy and surface tension forces and is defined as,

$$Eo = \frac{g\left(\rho_f - \rho_p\right)d_p^2}{\sigma}, \tag{21}$$

with σ being the surface tension. Note that Eo for rigid particles corresponds to $\sigma \to \infty$, so Eo is zero in our simulations which means Eq. (20) reduces to the famous Schiller–Naumann drag coefficient. In Eq. 20, Reynolds number is defined with the rise velocity of the particle as:

$$Re = \frac{\rho_f\left|\mathbf{V}\right|d_p}{\mu_f}. \tag{22}$$

The simulation setup is similar to the previous case (section 4.1.1) with $\rho_p/\rho_f = 0.001$ and different Ar to achieve different Reynolds number defined by the terminal velocity. Figure 3 shows the comparison of PUReIBM results with experimental results and the drag correlation in Eq. (20). The results of PUReIBM are presented for two grid resolutions, and it is clear that the finer grid gives the correct results at a higher Reynolds number. In general, the results of PUReIBM match very well with experiments and the correlation.
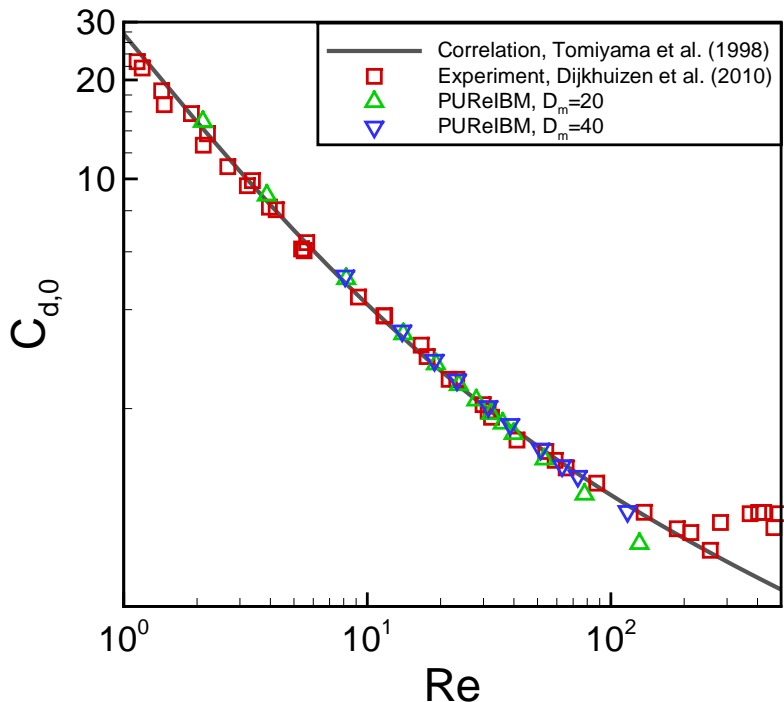
17

Figure 3: Drag coefficient versus Reynolds number from simulation of a single buoyant particle in PUReIBM compared with experimental results of a nearly spherical bubble in contaminated liquid [9] and drag correlation for a single bubble in contaminated liquid [65].

4.2. Rise of two buoyant particles

The next simulation that is presented is for the rise of two in-line particles. The particles rising in-line is a specific but typical case where mutual interactions between particles are evident. In this particular case, the rise velocity of the trailing particle is affected (and increased) by the wake of the leading particle. Finally, the trailing particle reaches the leading particle.

The simulation is again performed in a cuboidal domain with periodic boundary conditions in all directions. The length of the domain in the direction of gravity is $L_x = 89.6d_p$, which is 14 times the length of the domain in other directions. Similar to the single-particle case, the particles rise due to the buoyant force. The simulation is performed for a case with $Ar = 1700$, $\rho_p/\rho_f = 0.001$, $C_v = 0.15$, and the initial surface-to-surface distance between the particles is

18

$h_0/d_p = 11.6$. Figure 4(a) shows the rise velocity of particles versus surface-to-surface distance between them. The experimental results of Katz and Meneveau [66], shown in this figure, are for a similar case but bubbles in distilled water. For both the numerical and experimental cases, the Reynolds number based on the terminal velocity of a single particle/bubble is 35.4. Although the trend of the rise velocity in both cases is similar, they do not match. One reason for this is that the results of PUReIBM represent bubbles in contaminated liquid, while the experimental results are for bubbles in clean liquid. Note that Katz and Meneveau [66] used commercially available distilled water and not highly purified liquid, which could also be considered a partially contaminated liquid. Nevertheless, it is known that the drag force, and consequently, the rise velocity of bubbles in clean, partially contaminated, or contaminated is different. To have a better comparison, the rise velocity scaled by the rise velocity of a single particle/bubble is plotted in Fig. 4(b). With this scaling, it is easier to compare the relative velocity between the leading and trailing particle/bubble as a function of the distance between them since we have now a common basis for comparison in both cases ($|V|/V_{single} = 1$ at $h/d_p = 11.6$). This figure shows that the behavior of bubbles in contaminated or clean liquid is comparable if a proper scaling is used.
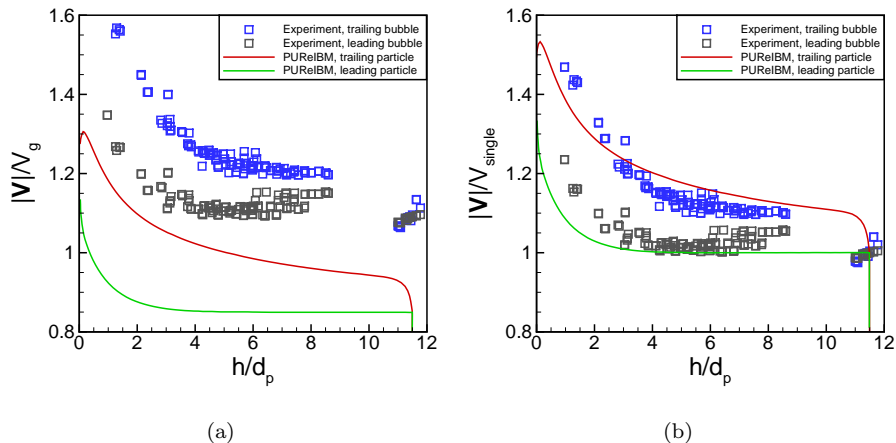
Figure 4: Rise velocity of two in-line particles from simulation in PUReIBM compared with experimental results of two in-line bubbles in distilled water [66]. (a) Rise velocity is scaled by the gravitational velocity. (b) Rise velocity is scaled by the rise velocity of a single particle/bubble.

4.3. Simulation of buoyant particle suspensions

The main goal of this paper is to perform simulations of buoyant particles at high volume fractions. In this section, the results of simulations for buoyant particle suspensions at volume fraction 0.1 to 0.4 are presented, and in particular, the drag force on the suspension is discussed.

4.3.1. Problem setup

In this part, the simulations are performed in a cubic domain with periodic boundary conditions. The initial positions of the particles are obtained following elastic collisions (in the absence of interstitial fluid), starting from a lattice arrangement with a Maxwellian velocity distribution. The particles and fluid are initially at rest and evolve under the action of gravity. A mean pressure gradient is imposed on the system to oppose the effect of gravity and keep the mean fluid velocity zero, and then the particle starts to move due to the buoyant force. The simulations are carried out until the mean particle velocity reaches a statistically stationary state. In our simulations, the mean drag on particles or mean particle velocity is computed by averaging over all particles

20

and then ensemble-averaging over different particle configurations. For each case, five independent realizations (corresponding to a specified initial particle configuration) are simulated in this study.

We have performed simulations for five different Ar and four different ϕ. The salient numerical and physical parameters used in the simulations are reported in Table 1. Note that the Reynolds number based on the rise velocity of the suspension Re is the outputs of the simulations. Note that an increase in volume fraction decreases the rise velocity (and the Reynolds number), as indicated in Table 1. In this Table, Re_0 is the Reynolds number of a single particle at each Ar number which is calculated by balancing the drag and buoyancy forces on a single particle which results in $Re_0^2 = 4\,Ar/\left(3\,C_{d,0}\right)$, where we have used Eq. (20) for the drag coefficient. For all cases density ratio is $\rho_p/\rho_f = 0.001$ and number of particle is $N_p = 200$. We have decreased the length of the domain by reducing the volume fraction to keep the number of particles fixed. The length of the domain is $L/d_p = 10.08, 8.06, 7.05, 6.4$ for $\phi = 0.1, 0.2, 0.3, 0.4$, respectively. The length of the domain is chosen to ensure that the two-point correlation functions in the fluid phase decay to zero within the box length [53]. The grid resolution used in this study is sufficient to obtain converged results for the mean drag and second moments of particle and fluid velocities.

Table 1: The numerical and physical parameters of the simulations: Archimedes number Ar, Reynolds number of a single particle Re_0, volume fraction of particles ϕ, the number of grid cells across the diameter of a particle $d_p/\Delta x$, Reynolds number of the suspensions Re. For all cases $N_p = 200$ and $\rho_p/\rho_f = 0.001$.

Ar	Re_0	ϕ	$d_p/\Delta x$	Re
5×10^3	72.33	$0.1, 0.2, 0.3, 0.4$	$30, 30, 30, 30$	$48.66, 37.96, 29.36, 21.13$
1×10^4	113.85	$0.1, 0.2, 0.3, 0.4$	$30, 30, 30, 30$	$78.28, 61.13, 47.16, 35.52$
2×10^4	177.43	$0.1, 0.2, 0.3, 0.4$	$30, 30, 30, 30$	$120.28, 95.81, 76.19, 57.14$
5×10^4	315.27	$0.1, 0.2, 0.3, 0.4$	$40, 40, 40, 40$	$206.21, 161.21, 135.17, 107.87$
1×10^5	483.82	$0.1, 0.2, 0.3, 0.4$	$50, 50, 40, 40$	$309.37, 256.88, 209.22, 161.25$

According to Eq. (9), C_v^{min} is related to the added mass coefficient. Many studies have shown that added mass coefficient increases with volume fraction [67–71]. Spelt and Sangani [72] also reported the same dependence, however, they included the effect of microstructure on the added mass through the velocity fluctuations of bubbles. On the other hand, Simcik et al. [49] and Simcik and Ruzicka [73] have reported that the added mass coefficient can decrease or increase with volume fraction depending on the shape of the computational domain. In our simulations, we have to increase C_v^{min} with volume fraction to get stable results, which indicates that the added mass coefficient increases with volume fraction.

In PUReIBM, C_v^{min} is found from numerical experiments to increase from 0.18 for $\phi = 0.1$ to 0.22 for $\phi = 0.4$. Using the correlation by Zuber [67], C_{am} increases from 0.66 for $\phi = 0.1$ to $C_{am} = 1.5$ for $\phi = 0.4$. It shows that the growth of C_v^{min} with volume fraction is slower than the growth of C_{am}. In this study, $C_v = 0.25$ is used for all volume fractions in the simulation of particle suspensions. It is also important to mention that there is no added mass effect in an average sense since the simulations reach a statistically stationary state; however, each individual particle experiences the added mass effect. Therefore, using the virtual force stabilization technique is necessary at any stage of the simulations.

4.3.2. Drag coefficient of the buoyant particle suspensions

The results presented in this section are the drag coefficient C_d of the buoyant particle suspensions obtained from PUReIBM, which are compared with experimental and numerical results for bubbly flows. The drag coefficient for the suspension is scaled with the drag coefficient of a single particle $C_{d,0}$ at the same Archimedes number multiplied with $(1 - \phi)$. As a result the scaled drag coefficient is equal to the squared of the ratio of the rise velocity of a single particle to the rise velocity of the suspensions, i.e. [74]:

$$\frac{C_d}{C_{d,0}\,(1 - \phi)} = \left(\frac{|\mathbf{V}_0|}{|\langle\mathbf{V}\rangle|}\right)^2 = \left(\frac{Re_0}{Re}\right)^2 = f. \tag{23}$$

22

In general, f could be a function of Re, ϕ, and Eo. However, if $C_{d,0}$ already incorporates the dependencies on Re and Eo, the function f would only depend on ϕ. Similarly, we can say that the comparison of f for clean and contaminated bubbles is only valid if the effect of contamination is considered in $C_{d,0}$. In other words, the drag of bubbles in clean and contaminated liquid is not comparable unless a proper scaling is used, as discussed in Section 4.2. For this reason, different studies have used $C_{d,0}$ from different correlations or measurements in Eq. (23) for reporting f. In this work, Eq. (20) is used for $C_{d,0}$ for scaling.

All the experimental correlations used in this paper for comparison only depend on the volume fraction (see Table 2). This means that experimental studies verify that the effects of Re and Eo are fully accounted for in $C_{d,0}$. The form of the correlation by Bridge et al. [75] is inspired by Richardson and Zaki [76]. Rusche and Issa [77] used data from different experimental works in the literature to propose their correlation. Their correlation is a rough fit to a lot of experimental data with large deviations for $5 \times 10^4 < Ar < 1 \times 10^7$. The highest Archimedes number in our simulations is $Ar = 1 \times 10^5$. Garnier et al. [78] performed their experiments in a highly controlled environment with a uniform swarm of monodisperse bubbles without recirculating motions in the liquid phase, and their correlation is also verified in experiments by Guet et al. [79]. Their correlation comes from experiments with $300 < Re < 500$.

Table 2: Experimental correlations for the scaled drag coefficient, i.e., function f in Eq. (23).

Correlation	Condition	Reference
$\left[(1-\phi)^{1.39} \right]^{-2}$	$\phi < 0.2$	Bridge et al. [75]
$\left[\exp\left(3.64\phi\right) + \phi^{0.864} \right] (1-\phi)^{-1}$	$\phi < 0.45$	Rusche and Issa [77]
$\left[1 - \phi^{1/3} \right]^{-2}$	$\phi < 0.3$	Garnier et al. [78]

The numerical correlations by Roghair et al. [74, 80] are obtained from FR-DNS using the front-tracking method (FTM) and depend on both volume frac-

tion and Eötvös number (see Table 3). Based on their work, it is concluded that only the effect of Re is incorporated in $C_{d,0}$ and not Eo. Our simulations of buoyant particles correspond to spherical bubbles in contaminated liquid at $Eo = 0$. So, our results in this section are compared with Roghair's second and third correlations since they are developed for smaller values of Eo.

Table 3: Numerical correlations by Roghair et al. [74, 80] for the scaled drag coefficient, i.e., function f in Eq. (23).

Correlation	Condition	Reference
$1 + \left(\dfrac{18}{Eo} \right) \phi$	wobbling bubbles $1.2 < Eo < 4.8$ $0.05 < \phi < 0.45$	Roghair et al. [74]
$1 + \left(\dfrac{22}{Eo + 0.4} \right) \phi$	spherical/wobbling bubbles $0.134 < Eo < 4.8$ $0.05 < \phi < 0.4$	Roghair et al. [80]
$1 + \left(\dfrac{6.612 Eo + 2.023}{Eo} \right) \phi$	spherical/ellipsoidal bubbles $0.5 < Eo < 2$ $0.05 < \phi < 0.15$	Roghair et al. [80]

Figure 5 compares the results for the scaled drag coefficient in buoyant particle suspensions and bubbly flows. The correlations are extended to higher volume fractions if the range for which they are proposed covers a smaller range. Our results in Fig. 5 show that the scaled drag coefficient depends on both Archimedes number (or equivalently Reynolds number) and volume fraction. However, there is a trend in the results, which shows that with increasing Ar the scaled drag becomes only a function of volume fraction. In other words, the data for higher Ar collapse to a single line. Nevertheless, it is interesting to note that the results of PUReIBM, similar to the experimental correlations, show a nonlinear dependence of drag coefficient on volume fraction. In contrast, all correlations of clean bubbles using FTM have linear dependence (see Table 3). Although Roghair et al. [74] do not provide the reason behind the linear nature

of their correlations, they raise four possible issues in their work including the effect of 1) contamination, 2) coalescence and breakup, 3) normalization with $C_{d,0}$ which comes from different correlations or measurements for each case, and 4) having a smaller computational domain in comparison to the large domain of experiments.

Of these, two limitations are addressed in this work. First, the bubbles in this study are contaminated bubbles, and the results of experimental works might also have some level of contamination. Secondly, the FR-DNS results from FTM by Roghair et al. [74, 80] can only take local gas fractions into account, since the computational domain is small compared to the physical domain typically used in experiments. In fact, Roghair et al. [74, 80] have between 16 to 32 bubbles for different simulations while 200 particles is used for each case in PUReIBM. Therefore, it is concluded that PUReIBM results have a similar trend to experiments since they are performed in larger domains with more particles.

It should also be mentioned that Simonnet et al. [81] developed a drag correlation using local volume fraction definition in their experiments, but their correlation predicts that the drag coefficient increases very slowly up to volume fraction 15% and then decreases with increasing volume fraction. The main reason for the different behavior they obtained is that the bubbles in their experiment are large ($d_b > 7mm$), and because of this, their correlation is not presented here.
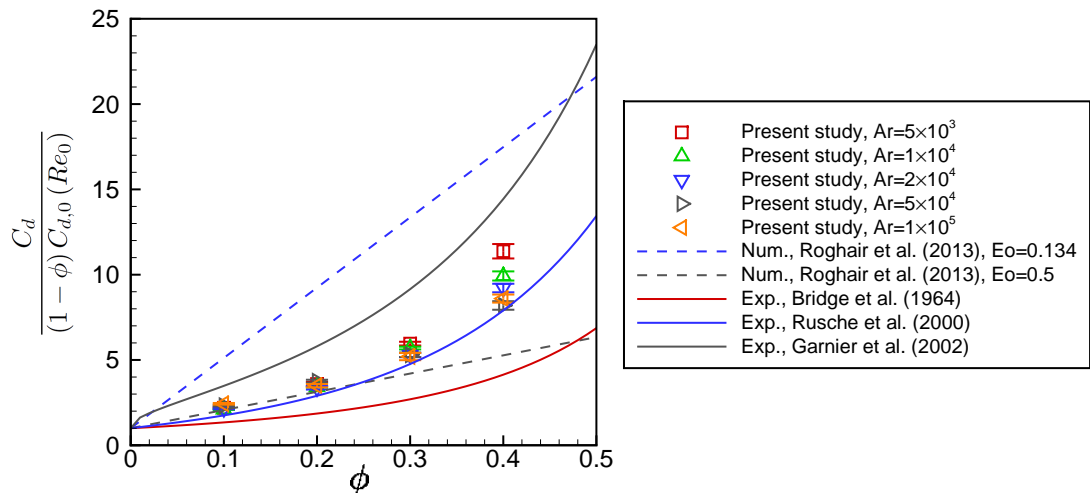
Figure 5: Comparison of drag coefficient of the suspension scaled with $C_{d,0}\,(Re_0)$ obtained from PUReIBM with different drag correlations. Solid lines are the correlations obtained from different experiments (see Table 2). Dashed lines are the correlations obtained from simulations using FTM [80] for two different values of Eo (see Table 3). Symbols are the scaled drag coefficients obtained from PUReIBM (present study) for different values of Ar. The error bars represent 95% confidence intervals obtained from five independent realizations for each case.

4.3.3. Drag correlation of the suspension

In general, fully resolved simulations are a useful tool for model development for macro-scale simulations [11]. For instance, drag force obtained from fully resolved simulation has been already used to develop a model for interphase momentum transfer in two-fluid equations [16–18, 53, 82]. Similarly, we can propose a correlation for the drag coefficient using our data presented in Fig. 5. However, a correlation based on this data set will be a function of both Ar (or Re) and ϕ. Interestingly, if we scale the drag coefficient of the suspension with the drag coefficient of a single particle at the same Reynolds number of the suspension (instead of the drag coefficient of a single particle at the same Archimedes number of the suspension which results in Re_0 reported in Table 1), all data collapse to a single line. In other words, in this new scaling, we calculate

26

$C_{d,0}$ from Eq. (20) with Re_m instead of Re_0 where Re_m is the Reynolds number based on the superficial velocity of the suspensions:

$$Re_m = (1 - \phi) Re = \frac{\rho_f (1 - \phi) |\langle \mathbf{V} \rangle| d_p}{\mu_f}. \tag{24}$$

The results with both scaling are shown in Fig. 6. Using the Reynolds number of the suspension in correlations of drag law is common and several other correlations for gas–solid flows (fixed bed or freely evolving) are proposed based on the Reynolds number with mean slip velocity in the suspension[53, 82–88]. Since our results with this new scaling are not affected by Ar significantly, the scaled drag coefficient is modeled here as only a function of volume fraction. We propose the following correlation by curve fitting (with $R^2 = 0.9903$):

$$\frac{C_d}{(1 - \phi) C_{d,0} (Re_m)} = 48.51\phi^3 - 24.15\phi^2 + 9.81\phi + 1. \tag{25}$$

Note that in developing this correlation, we have used the fact that this ratio should be unity at $\phi = 0$.
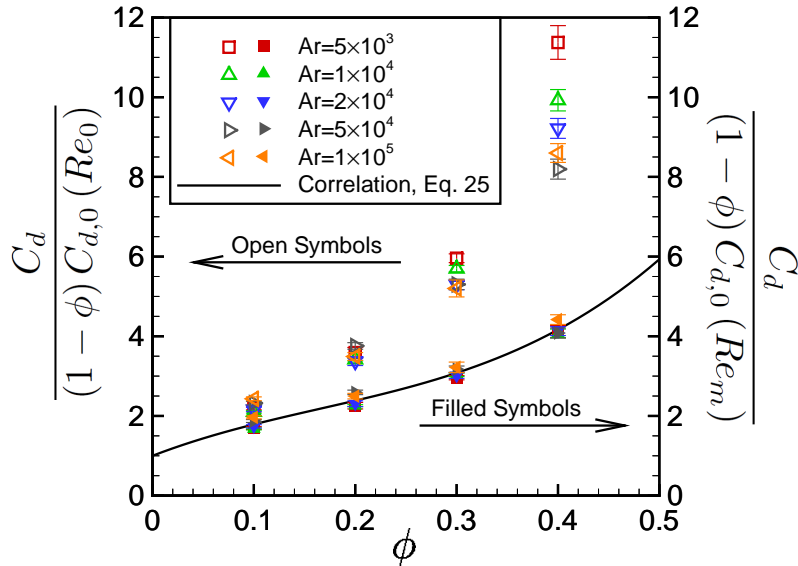
Figure 6: Drag coefficient of the suspension scaled with $C_{d,0}(Re_0)$ (empty symbols) and $C_{d,0}(Re_m)$ (filled symbols) obtained from PUReIBM (present study) for different values of Ar. Solid line is the correlation developed (Eq. 25) based on scaling with $C_{d,0}(Re_m)$. The error bars represent 95% confidence intervals obtained from five independent realizations for each case.

FR-DNS can also be used to develop stochastic or deterministic models of acceleration in point-particle simulations [52, 55, 89, 90] or for model development in Euler–Lagrange simulation where Eulerian equations are volume filtered [91]. This work opens the door to the development of such models for buoyant particles in future studies.

5. Conclusions

In this work, a FR-DNS solver based on PUReIBM is developed for simulation of buoyant particles with a density ratio as small as 0.001 and for a range of volume fraction up to 40%. It is explained that when the mass of a particle is smaller than the added mass induced by the surrounding fluid, explicit numerical methods are unstable. To stabilize the method, the virtual force technique introduced by Schwarz et al. [46] is extended. It is shown that

the virtual force constant C_v has a lower limit for having stable simulations, which depends on the density ratio and the added mass coefficient. Since the added mass coefficient increases with an increase in the volume fraction of particles, it is concluded that C_v should also increase in the case of buoyant particle suspensions when compared to the single-particle case.

Simulations of rigid buoyant particles are performed, which are considered a good approximation for bubbles in contaminated liquid. The results from simulations of a single buoyant particle at different Archimedes number are presented and compared with the numerical and experimental reference data to validate the implementation of the virtual force in PUReIBM. Then two in-line rising buoyant particles are simulated and compared with experimental results. Finally, simulations of freely evolving buoyant particle suspensions are presented. The scaled drag coefficient of particle suspensions at different volume fractions are compared with numerical and experimental correlations of bubbly flows from the literature. It is shown the increase in the scaled drag coefficient of buoyant particles with volume fraction from FR-DNS using PUReIBM matches the nonlinear trend in experimental data of bubbly flows, while the correlations from FR-DNS using FTM by Roghair et al. [74, 80] predict a linear increase. They hypothesized that this linear dependence could be to the fact that their bubbles are in clean liquid, and their simulations are performed for a small domain with 16 up to 32 bubbles in it. It is shown here that considering a larger domain with 200 buoyant particles (bubbles in contaminated liquid) predicts the nonlinear behavior seen in experimental studies. Finally, it is shown that scaling the drag coefficient of the suspension with the drag coefficient of a single particle at the same Reynolds number of the suspension is only a function of the volume fraction and a drag correlation is presented based on data using this scaling.

Acknowledgments

Appendix A. Numerical calculation of virtual force and torque

As explained in section 3.1, one needs to numerically calculate $\mathbf{F}_v$ and $\mathbf{T}_v$ on the right-hand side of Eqs. (16) and (17) before numerically integrate them to calculate $\mathbf{V}$ and $\boldsymbol{\Omega}$ in time. In this Appendix, we explain how it is done for virtual force. The same approach is used for virtual torque. Eq. (16) can be re-written as:

$$\frac{d\mathbf{V}}{dt} = \alpha_f \boldsymbol{\xi}_f + \alpha_v \boldsymbol{\xi}_v, \tag{A.1}$$

where $\alpha_f = \dfrac{1}{\left(\rho_p + C_v \rho_f\right) V_p}$, $\boldsymbol{\xi}_f = \mathbf{F}_B + \mathbf{F}_h + \displaystyle\sum_{\substack{j=1 \\ j \neq i}}^{N_p} \mathbf{F}_c^{(ij)}$, $\alpha_v = \dfrac{C_v \rho_f}{\rho_p + C_v \rho_f}$, $\boldsymbol{\xi}_v = \dfrac{d\mathbf{V}}{dt}$.

The following method which is a combination of the Adams-Bashforth predictor-corrector scheme and the trapezoidal rule is used to approximate $\boldsymbol{\xi}_v$ and then update the velocity:

$$\boldsymbol{\xi}_v^n = \frac{3\mathbf{V}^n - 4\mathbf{V}^{n-1} + \mathbf{V}^{n-2}}{2\Delta t}$$

$$\tilde{\boldsymbol{\xi}}^n = \alpha_f \boldsymbol{\xi}_f^n + \alpha_v \boldsymbol{\xi}_v^n$$

$$\mathbf{V}_{pred}^{n+1} = \mathbf{V}^n + \frac{\Delta t}{2}\left(3\tilde{\boldsymbol{\xi}}^n - \tilde{\boldsymbol{\xi}}^{n-1}\right)$$

$$\boldsymbol{\xi}_{v,pred}^{n+1} = \frac{3\mathbf{V}_{pred}^{n+1} - 4\mathbf{V}^n + \mathbf{V}^{n-1}}{2\Delta t}$$

$$\boldsymbol{\xi}_v^{n+\frac{1}{2}} = \frac{1}{2}\left(\boldsymbol{\xi}_v^n + \boldsymbol{\xi}_{v,pred}^{n+1}\right)$$

$$\mathbf{V}^{n+1} = \mathbf{V}^n + \Delta t \left(\alpha_f \boldsymbol{\xi}_f^n + \alpha_a \boldsymbol{\xi}_v^{n+\frac{1}{2}}\right) \tag{A.2}$$

Appendix B. Rise of a single buoyant particle in an inclined channel

Here the rise of a buoyant particle in an inclined channel is simulated, which corresponds to the experiment by Lomholt et al. [64]. The particle rises in this inclined channel due to buoyancy and travels alongside the right wall of the domain. The simulation is performed for a particle with $\rho_p/\rho_f = 0.97$, which is the same as experimental work. For this density ratio, PUReIBM works properly even without the virtual force stabilization technique. As mentioned earlier, the lowest density ratio that PUReIBM becomes unstable without using

virtual force is $\rho_p/\rho_f = 0.07$. In other words, the results with and without virtual force would be the same for $\rho_p/\rho_f = 0.97$. Since this test case is a general validation for PUReIBM, we have presented it in this appendix. The experiment is performed for $Re_p^{Stokes} = 13.6$ which is the Reynolds number based on the Stokes settling velocity W and is defined as

$$Re_p^{Stokes} = \frac{W d_p}{\nu} = \frac{d_p^3}{18\nu}|\frac{\rho_p}{\rho_f} - 1|g. \tag{B.1}$$

It is clear from Eq. (19) that $Ar = 18\ Re_p^{Stokes}$. For comparison, we have performed the simulation at $Ar = 244.8$. The channel is inclined at an angle of $8.23°$ with the vertical. Numerically, this is simulated by adding components of gravitational forces in the horizontal and vertical directions. The computational domain consists of a rectangular box $L/d_p = (20, 5, 40)$. The grid is Cartesian and uniform over the domain with $d_p/\Delta x = 20$. The particle is injected at $\mathbf{x}_0/d_p = (10, 1.8, -0.5)$.

The numerical method used in PUReIBM to solve Navier–Stokes equations is a pseudo-spectral method with Fourier basis functions. This means that we can only impose periodic boundary conditions in our code (and not the no-slip boundary condition for the wall). However, we can simulate a wall (imposing no-slip boundary condition on a plane) using the immersed boundary approach itself. We have done this already for single-phase flow [51] and heat transfer Tenneti et al. [92] in a duct. Therefore, the periodic boundary condition is imposed in all directions, and a wall is generated in $xz-$plane at $y/d_p = 5$ using the immersed boundary method. Although we only generate the wall at one location, due to the periodic boundary condition, this will result in the creation of a channel.

Fig. B.7 compares the results from PUReIBM and experimental work and numerical modeling using force coupling method by [64].
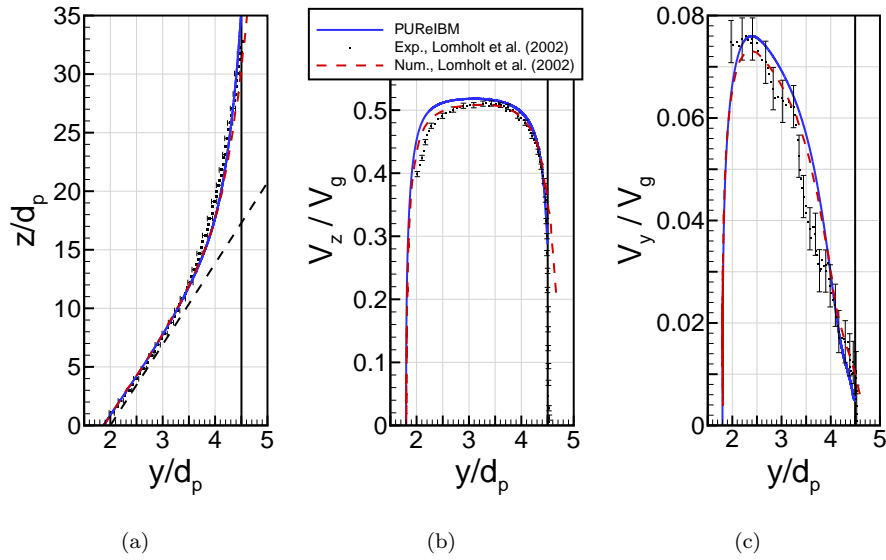
Figure B.7: Comparison of predicted results by the present scheme with the experimental study and numerical modeling using force coupling method by Lomholt et al. [64]. A solid vertical line at $y/d_p = 4.5$ represents the distance of one particle radius from the wall. (a) Particle trajectory (dashed line shows the gravity direction). (b) Velocity of the particle in the vertical direction. (c) Velocity of the particle in the lateral direction.

References

References

[1] Wright SL, Thompson RC, Galloway TS. The physical impacts of microplastics on marine organisms: A review. Environ Pollut 2013;178:483–92. doi:10.1016/j.envpol.2013.02.031.

[2] Driedger AG, Dürr HH, Mitchell K, Cappellen PV. Plastic debris in the laurentian great lakes: A review. J Great Lakes Res 2015;41(1):9–19. doi:10.1016/j.jglr.2014.12.020.

[3] Clift R, Grace JR, Weber ME. Bubbles, drops, and particles. New York: Academic Press; 1978.

[4] Magnaudet J, Eames I. The motion of high-Reynolds-number bubbles in inhomogeneous flows. Annu Rev Fluid Mech 2000;32(1):659–708. doi:10.1146/annurev.fluid.32.1.659.

[5] Takagi S, Matsumoto Y. Surfactant effects on bubble motion and bubbly flows. Annu Rev Fluid Mech 2011;43(1):615–36. doi:10.1146/annurev-fluid-122109-160756.

[6] Sridhar G, Katz J. Drag and lift forces on microscopic bubbles entrained by a vortex. Phys Fluids 1995;7(2):389–99. doi:10.1063/1.868637.

[7] Bel Fdhila R, Duineveld PC. The effect of surfactant on the rise of a spherical bubble at high Reynolds and Peclet numbers. Phys Fluids 1996;8(2):310–21. doi:10.1063/1.868787.

[8] Cartellier A, Riviére N. Bubble-induced agitation and microstructure in uniform bubbly flows at small to moderate particle Reynolds numbers. Phys Fluids 2001;13(8):2165–81. doi:10.1063/1.1381562.

[9] Dijkhuizen W, Roghair I, Annaland MVS, Kuipers J. DNS of gas bubbles behaviour using an improved 3D front tracking model—Drag force on isolated bubbles and comparison with experiments. Chem Eng Sci 2010;65(4):1415–26. doi:10.1016/j.ces.2009.10.021.

[10] Peters F, Els C. An experimental study on slow and fast bubbles in tap water. Chem Eng Sci 2012;82:194–9. doi:10.1016/j.ces.2012.06.061.

[11] Tenneti S, Subramaniam S. Particle-resolved direct numerical simulation for gas–solid flow model development. Annu Rev Fluid Mech 2014;46(1):199–230. doi:10.1146/annurev-fluid-010313-141344.

[12] Uhlmann M. An immersed boundary method with direct forcing for the simulation of particulate flows. J Comput Phys 2005;209(2):448–76. doi:10.1016/j.jcp.2005.03.017.

[13] Tenneti S, Garg R, Hrenya C, Fox R, Subramaniam S. Direct numerical simulation of gas–solid suspensions at moderate Reynolds number: Quantifying the coupling between hydrodynamic forces and particle velocity fluctuations. Powder Technol 2010;203(1):57–69. doi:10.1016/j.powtec.2010.03.042.

[14] Kempe T, Fröhlich J. An improved immersed boundary method with direct forcing for the simulation of particle laden flows. J Comput Phys 2012;231(9):3663–84. doi:10.1016/j.jcp.2012.01.021.

[15] Breugem WP. A second-order accurate immersed boundary method for fully resolved simulations of particle-laden flows. J Comput Phys 2012;231(13):4469–98. doi:10.1016/j.jcp.2012.02.026.

[16] Hill RJ, Koch DL, Ladd AJC. The first effects of fluid inertia on flows in ordered and random arrays of spheres. J Fluid Mech 2001;448:213–41. doi:10.1017/S0022112001005948.

[17] Hill RJ, Koch DL, Ladd AJC. Moderate-Reynolds-number flows in ordered and random arrays of spheres. J Fluid Mech 2001;448:243–78. doi:10.1017/S0022112001005936.

[18] van der Hoef MA, Beetstra R, Kuipers JAM. Lattice-Boltzmann simulations of low-Reynolds-number flow past mono- and bidisperse arrays of spheres: Results for the permeability and drag force. J Fluid Mech 2005;528:233–54. doi:10.1017/S0022112004003295.

[19] Yin X, Koch DL. Hindered settling velocity and microstructure in suspensions of solid spheres with moderate reynolds numbers. Phys Fluids 2007;19(9):093302. doi:10.1063/1.2764109.

[20] Yin X, Koch DL. Lattice-Boltzmann simulation of finite Reynolds number buoyancy-driven bubbly flows in periodic and wall-bounded domains. Phys Fluids 2008;20(10):103304. doi:10.1063/1.3001728.

[21] Glowinski R, Pan TW, Hesla T, Joseph D. A distributed Lagrange multiplier/fictitious domain method for particulate flows. Int J Multiphase Flow 1999;25(5):755–94. doi:`10.1016/S0301-9322(98)00048-2`.

[22] Sharma N, Patankar NA. A fast computation technique for the direct numerical simulation of rigid particulate flows. J Comput Phys 2005;205(2):439–57. doi:`10.1016/j.jcp.2004.11.012`.

[23] Yu Z, Shao X, Wachs A. A fictitious domain method for particulate flows with heat transfer. J Comput Phys 2006;217(2):424–52. doi:`10.1016/j.jcp.2006.01.016`.

[24] Apte SV, Martin M, Patankar NA. A numerical method for fully resolved simulation (FRS) of rigid particle–flow interactions in complex flows. J Comput Phys 2009;228(8):2712–38. doi:`10.1016/j.jcp.2008.11.034`.

[25] Apte SV, Finn JR. A variable-density fictitious domain method for particulate flows with broad range of particle–fluid density ratios. J Comput Phys 2013;243:109–29. doi:`10.1016/j.jcp.2012.12.021`.

[26] Zhang Z, Prosperetti A. A second-order method for three-dimensional particle simulation. J Comput Phys 2005;210(1):292–324. doi:`10.1016/j.jcp.2005.04.009`.

[27] Sierakowski AJ, Prosperetti A. Resolved-particle simulation by the Physalis method: Enhancements and new capabilities. J Comput Phys 2016;309:164–84. doi:`10.1016/j.jcp.2015.12.057`.

[28] Hu HH, Patankar N, Zhu M. Direct numerical simulations of fluid–solid systems using the arbitrary Lagrangian–Eulerian technique. J Comput Phys 2001;169(2):427–62. doi:`10.1006/jcph.2000.6592`.

[29] Burton TM, Eaton JK. Fully resolved simulations of particle-turbulence interaction. J Fluid Mech 2005;545:67–111. doi:`10.1017/S0022112005006889`.

[30] Bagchi P, Balachandar S. Effect of free rotation on the motion of a solid sphere in linear shear flow at moderate Re. Phys Fluids 2002;14(8):2719–37. doi:10.1063/1.1487378.

[31] Bagchi P, Balachandar S. Shear versus vortex-induced lift force on a rigid sphere at moderate Re. J Fluid Mech 2002;473:379–88. doi:10.1017/S0022112002002628.

[32] Inamuro T, Ogata T, Tajima S, Konishi N. A lattice Boltzmann method for incompressible two-phase flows with large density differences. J Comput Phys 2004;198(2):628–44. doi:10.1016/j.jcp.2004.01.019.

[33] Yang J, Stern F. A sharp interface direct forcing immersed boundary approach for fully resolved simulations of particulate flows. ASME J Fluids Eng 2014;136(4):040904. doi:10.1115/1.4026198.

[34] Maxey M. Simulation methods for particulate flows and concentrated suspensions. Annu Rev Fluid Mech 2017;49(1):171–93. doi:10.1146/annurev-fluid-122414-034408.

[35] Causin P, Gerbeau J, Nobile F. Added-mass effect in the design of partitioned algorithms for fluid–structure problems. Comput Methods Appl Mech Eng 2005;194(42):4506–27. doi:10.1016/j.cma.2004.12.005.

[36] Förster C, Wall WA, Ramm E. Artificial added mass instabilities in sequential staggered coupling of nonlinear structures and incompressible viscous flows. Comput Methods Appl Mech Eng 2007;196(7):1278–93. doi:10.1016/j.cma.2006.09.002.

[37] Borazjani I, Ge L, Sotiropoulos F. Curvilinear immersed boundary method for simulating fluid structure interaction with complex 3D rigid bodies. J Comput Phys 2008;227(16):7587–620. doi:10.1016/j.jcp.2008.04.028.

[38] Sotiropoulos F, Yang X. Immersed boundary methods for simulating fluid–structure interaction. Prog Aerosp Sci 2014;65:1–21. doi:10.1016/j.paerosci.2013.09.003.

[39] Fernández MÁ, Moubachir M. A Newton method using exact jacobians for solving fluid–structure coupling. Comput Struct 2005;83(2):127–42. doi:`10.1016/j.compstruc.2004.04.021`; Advances in Analysis of Fluid Structure Interaction.

[40] Figueroa CA, Vignon-Clementel IE, Jansen KE, Hughes TJ, Taylor CA. A coupled momentum method for modeling blood flow in three-dimensional deformable arteries. Comput Methods Appl Mech Eng 2006;195(41):5685–706. doi:`10.1016/j.cma.2005.11.011`; John H. Argyris Memorial Issue. Part II.

[41] Tallec PL, Mouro J. Fluid structure interaction with large structural displacements. Comput Methods Appl Mech Eng 2001;190(24):3039–67. doi:`10.1016/S0045-7825(00)00381-9`; Advances in Computational Methods for Fluid–Structure Interaction.

[42] Burman E, Fernández MA. Stabilization of explicit coupling in fluid–structure interaction involving fluid incompressibility. Comput Methods Appl Mech Eng 2009;198(5):766–84. doi:`10.1016/j.cma.2008.10.012`.

[43] Guidoboni G, Glowinski R, Cavallini N, Canic S. Stable loosely-coupled-type algorithm for fluid–structure interaction in blood flow. J Comput Phys 2009;228(18):6916–37. doi:`10.1016/j.jcp.2009.06.007`.

[44] Garg R, Tenneti S, Mohd-Yusof J, Subramaniam S. Direct numerical simulation of gas–solids flow based on the immersed boundary method. In: Pannala S, Syamlal M, O'Brien TJ, editors. Computational Gas–Solids Flows and Reacting Systems: Theory, Methods and Practice. Hershey, PA: IGI Global; 2011, p. 245–76. doi:`10.4018/978-1-61520-651-3.ch008`.

[45] Tschisgale S, Kempe T, Fröhlich J. A non-iterative immersed boundary method for spherical particles of arbitrary density ratio. J Comput Phys 2017;339:432–52. doi:`10.1016/j.jcp.2017.03.026`.

[46] Schwarz S, Kempe T, Fröhlich J. A temporal discretization scheme to compute the motion of light particles in viscous flows by an immersed boundary method. J Comput Phys 2015;281:591–613. doi:`10.1016/j.jcp.2014.10.039`.

[47] Santarelli C, Fröhlich J. Direct numerical simulations of spherical bubbles in vertical turbulent channel flow. Int J Multiphase Flow 2015;75:174–93. doi:`10.1016/j.ijmultiphaseflow.2015.05.007`.

[48] Xia Y, Yu Z, Deng J. A fictitious domain method for particulate flows of arbitrary density ratio. Comput Fluids 2019;193:104293. doi:`10.1016/j.compfluid.2019.104293`.

[49] Simcik M, Ruzicka M, Drahoš J. Computing the added mass of dispersed particles. Chem Eng Sci 2008;63(18):4580–95. doi:`10.1016/j.ces.2008.06.011`.

[50] Mohd-Yusof J. Interaction of massive particles with turbulence. Ph.D. thesis; Cornell University; 1996.

[51] Mehrabadi M, Tenneti S, Garg R, Subramaniam S. Pseudo-turbulent gas-phase velocity fluctuations in homogeneous gas–solid flow: Fixed particle assemblies and freely evolving suspensions. J Fluid Mech 2015;770:210–46. doi:`10.1017/jfm.2015.146`.

[52] Tenneti S, Mehrabadi M, Subramaniam S. Stochastic Lagrangian model for hydrodynamic acceleration of inertial particles in gas–solid suspensions. J Fluid Mech 2016;788:695–729. doi:`10.1017/jfm.2015.693`.

[53] Tenneti S, Garg R, Subramaniam S. Drag law for monodisperse gas–solid systems using particle-resolved direct numerical simulation of flow past fixed assemblies of spheres. Int J Multiphase Flow 2011;37(9):1072–92. doi:`10.1016/j.ijmultiphaseflow.2011.05.010`.

[54] Cundall PA, Strack ODL. A discrete numerical model for granular assemblies. Géotechnique 1979;29(1):47–65. doi:`10.1680/geot.1979.29.1.47`.

[55] Akiki G, Moore W, Balachandar S. Pairwise-interaction extended point-particle model for particle-laden flows. J Comput Phys 2017;351:329–57. doi:10.1016/j.jcp.2017.07.056.

[56] Tavanashad V, Passalacqua A, Fox RO, Subramaniam S. Effect of density ratio on velocity fluctuations in dispersed multiphase flow from simulations of finite-size particles. Acta Mech 2019;230:469–84. doi:10.1007/s00707-018-2267-3.

[57] Simeonov JA, Calantoni J. Modeling mechanical contact and lubrication in direct numerical simulations of colliding particles. Int J Multiphase Flow 2012;46:38–53. doi:10.1016/j.ijmultiphaseflow.2012.05.008.

[58] Jenny M, Dušek J. Efficient numerical method for the direct numerical simulation of the flow past a single light moving spherical body in transitional regimes. J Comput Phys 2004;194(1):215–32. doi:10.1016/j.jcp.2003.09.004.

[59] Jenny M, Dušek J, Bouchet G. Instabilities and transition of a sphere falling or ascending freely in a Newtonian fluid. J Fluid Mech 2004;508:201–39. doi:10.1017/S0022112004009164.

[60] Karamanev DG, Chavarie C, Mayer RC. Dynamics of the free rise of a light solid sphere in liquid. AIChE J 1996;42(6):1789–92. doi:10.1002/aic.690420630.

[61] Veldhuis C, Biesheuvel A, Lohse D. Freely rising light solid spheres. Int J Multiphase Flow 2009;35(4):312–22. doi:10.1016/j.ijmultiphaseflow.2009.01.005.

[62] Horowitz M, Williamson CHK. The effect of Reynolds number on the dynamics and wakes of freely rising and falling spheres. J Fluid Mech 2010;651:251–94. doi:10.1017/S0022112009993934.

[63] Rahmani M, Wachs A. Free falling and rising of spherical and angular particles. Phys Fluids 2014;26(8):083301. doi:10.1063/1.4892840.

[64] Lomholt S, Stenum B, Maxey M. Experimental verification of the force coupling method for particulate flows. Int J Multiphase Flow 2002;28(2):225–46. doi:10.1016/S0301-9322(01)00045-3.

[65] Tomiyama A, Kataoka I, Zun I, Sakaguchi T. Drag coefficients of single bubbles under normal and micro gravity conditions. JSME Int J Ser B 1998;41(2):472–9. doi:10.1299/jsmeb.41.472.

[66] Katz J, Meneveau C. Wake-induced relative motion of bubbles rising in line. Int J Multiphase Flow 1996;22(2):239–58. doi:10.1016/0301-9322(95)00081-X.

[67] Zuber N. On the dispersed two-phase flow in the laminar flow regime. Chem Eng Sci 1964;19(11):897–917. doi:10.1016/0009-2509(64)85067-3.

[68] Wijngaarden LV, Jeffrey DJ. Hydrodynamic interaction between gas bubbles in liquid. J Fluid Mech 1976;77(1):27–44. doi:10.1017/S0022112076001110.

[69] Biesheuvel A, Spoelstra S. The added mass coefficient of a dispersion of spherical gas bubbles in liquid. Int J Multiphase Flow 1989;15(6):911–24. doi:10.1016/0301-9322(89)90020-7.

[70] Sankaranarayanan K, Shan X, Kevrekidis IG, Sundaresan S. Analysis of drag and virtual mass forces in bubbly suspensions using an implicit formulation of the lattice Boltzmann method. J Fluid Mech 2002;452:61–96. doi:10.1017/S0022112001006619.

[71] Béguin C, Pelletier É, Étienne S. Void fraction influence on added mass in a bubbly flow. Eur J Mech B/Fluids 2016;56:28–45. doi:10.1016/j.euromechflu.2015.11.008.

[72] Spelt PD, Sangani AS. Properties and averaged equations for flows of bubbly liquids. Appl Sci Res 1997;58(1):337–86. doi:10.1023/A:1000856308915.

[73] Simcik M, Ruzicka M. Added mass of dispersed particles by CFD: Further results. Chem Eng Sci 2013;97:366–75. doi:`10.1016/j.ces.2013.04.041`.

[74] Roghair I, Lau Y, Deen N, Slagter H, Baltussen M, Annaland MVS, et al. On the drag force of bubbles in bubble swarms at intermediate and high Reynolds numbers. Chem Eng Sci 2011;66(14):3204–11. doi:`10.1016/j.ces.2011.02.030`.

[75] Bridge AG, Lapidus L, Elgin JC. The mechanics of vertical gas–liquid fluidized system I: Countercurrent flow. AIChE J 1964;10(6):819–26. doi:`10.1002/aic.690100610`.

[76] Richardson J, Zaki W. The sedimentation of a suspension of uniform spheres under conditions of viscous flow. Chem Eng Sci 1954;3(2):65–73. doi:`10.1016/0009-2509(54)85015-9`.

[77] Rusche H, Issa R. The effect of voidage on the drag force on particles, droplets and bubbles in dispersed two-phase flow. In: Japanese European Two-Phase Flow Meeting. Tsukuba, Japan; 2000,.

[78] Garnier C, Lance M, Mari J. Measurement of local flow characteristics in buoyancy-driven bubbly flow at high void fraction. Exp Therm Fluid Sci 2002;26(6):811–5. doi:`10.1016/S0894-1777(02)00198-X`.

[79] Guet S, Ooms G, Oliemans R, Mudde R. Bubble size effect on low liquid input drift–flux parameters. Chem Eng Sci 2004;59(16):3315–29. doi:`10.1016/j.ces.2004.03.036`.

[80] Roghair I, Van Sint Annaland M, Kuipers HJAM. Drag force and clustering in bubble swarms. AIChE J 2013;59(5):1791–800. doi:`10.1002/aic.13949`.

[81] Simonnet M, Gentric C, Olmos E, Midoux N. Experimental determination of the drag coefficient in a swarm of bubbles. Chem Eng Sci 2007;62(3):858–66. doi:`10.1016/j.ces.2006.10.012`.

[82] Beetstra R, van der Hoef MA, Kuipers JAM. Drag force of intermediate Reynolds number flow past mono- and bidisperse arrays of spheres. AIChE J 2007;53(2):489–501. doi:10.1002/aic.11065.

[83] Wen CY, Yu YH. Mechanics of fluidization. Chem Eng Prog Symp Ser 1966;62:100–11.

[84] Zaidi AA, Tsuji T, Tanaka T. A new relation of drag force for high Stokes number monodisperse spheres by direct numerical simulation. Adv Powder Technol 2014;25(6):1860–71. doi:10.1016/j.apt.2014.07.019.

[85] Bogner S, Mohanty S, Rüde U. Drag correlation for dilute and moderately dense fluid-particle systems using the lattice Boltzmann method. Int J Multiphase Flow 2015;68:71–9. doi:10.1016/j.ijmultiphaseflow.2014.10.001.

[86] Tang Y, Peters EAJF, Kuipers JAM, Kriebitzsch SHL, van der Hoef MA. A new drag correlation from fully resolved simulations of flow past monodisperse static arrays of spheres. AIChE J 2015;61(2):688–98. doi:10.1002/aic.14645.

[87] Tang Y, Peters EAJF, Kuipers JAM. Direct numerical simulations of dynamic gas–solid suspensions. AIChE J 2016;62(6):1958–69. doi:10.1002/aic.15197.

[88] Zaidi AA. Study of particle inertia effects on drag force of finite sized particles in settling process. Chem Eng Res Des 2018;132:714–28. doi:10.1016/j.cherd.2018.02.013.

[89] Akiki G, Jackson TL, Balachandar S. Pairwise interaction extended point-ticle model for a random array of monodisperse spheres. J Fluid Mech 2017;813:882–928. doi:10.1017/jfm.2016.877.

[90] Esteghamatian A, Euzenat F, Hammouti A, Lance M, Wachs A. A stochastic formulation for the drag force based on multiscale numeri-

cal simulation of fluidized beds. Int J Multiphase Flow 2018;99:363–82. doi:10.1016/j.ijmultiphaseflow.2017.11.003.

[91] Capecelatro J, Desjardins O. An Euler–Lagrange strategy for simulating particle-laden flows. J Comput Phys 2013;238:1–31. doi:10.1016/j.jcp.2012.12.015.

[92] Tenneti S, Sun B, Garg R, Subramaniam S. Role of fluid heating in dense gassolid flow as revealed by particle-resolved direct numerical simulation. Int J Heat Mass Transfer 2013;58(1):471–9. doi:10.1016/j.ijheatmasstransfer.2012.11.006.